A&A 594, A114 (2016)
DOI: 10.1051/0004-6361/201628997

Astronomy & Astrophysics

Radio continuum and X-ray emission from the most extreme far-IR-excess galaxy NGC 1377

An extremely obscured AGN revealed

F. Costagliola[1,2], R. Herrero-Illana[3], A. Lohfink[4], M. Pérez-Torres[3,5], S. Aalto[1], S. Muller[1], and A. Alberdi[3]

[1] Chalmers University of Technology, Onsala Space Observatory, 439 92 Onsala, Sweden
e-mail: costagli@chalmers.se
[2] INAF−Istituto di Radioastronomia – Italian ARC, via Gobetti 101, 40129 Bologna, Italy
[3] Instituto de Astrofísica de Andalucía (IAA-CSIC), Glorieta de la Astronomía, s/n, 18008 Granada, Spain
[4] Institute of Astronomy, University of Cambridge, Madingley Road, Cambridge CB30HA, UK
[5] Visiting Scientist: Departamento de Física Teorica, Facultad de Ciencias, Universidad de Zaragoza, 50009 Zaragoza, Spain

Received 25 May 2016 / Accepted 8 July 2016

ABSTRACT

Context. Galaxies which strongly deviate from the radio-far infrared (FIR) correlation are of great importance for studies of galaxy evolution as they may be tracing early, short-lived stages of starbursts and active galactic nuclei (AGNs). The most extreme FIR-excess galaxy NGC 1377 has long been interpreted as a young dusty starburst, but millimeter observations of CO lines revealed a powerful collimated molecular outflow which cannot be explained by star formation alone.
Aims. This paper aims to determine the nature of the energy source in the nucleus of NGC 1377 and to study the driving mechanism of the collimated CO outflow.
Methods. We present new radio observations of NGC 1377 at 1.5 and 10 GHz obtained with the *Jansky* Very Large Array (JVLA) and *Chandra* X-ray observations. The observations are compared to synthetic starburst models to constrain the properties of the central energy source.
Results. We obtained the first detection of the cm radio continuum and X-ray emission in NGC 1377. We found that the radio emission is distributed in two components, one on the nucleus and another offset by 4.″5 to the south-west. We confirm the extreme FIR-excess of the galaxy, with a $q_{\rm FIR} \simeq 4.2$, which deviates by more than 7σ from the radio-FIR correlation. Soft X-ray emission is detected on the off-nucleus component. From the radio emission we estimated for a young (<10 Myr) starburst a star formation rate (SFR) of <0.1 $M_\odot$ yr^{-1}. Such a SFR is not sufficient to power the observed IR luminosity and to drive the CO outflow.
Conclusions. We found that a young starburst cannot reproduce all the observed properties of the nucleus of NGC 1377. We suggest that the galaxy may be harboring a radio-quiet, obscured AGN of 10^6 $M_\odot$, accreting at near-Eddington rates. We speculate that the off-nucleus component may be tracing an hot-spot in the AGN jet.

Key words. radio continuum: galaxies – X-rays: galaxies – galaxies: active – galaxies: starburst – galaxies: jets – galaxies: individual: NGC 1377

1. Introduction

A small fraction of galaxies (e.g., Helou et al. 1985) have faint radio and bright far-infrared (FIR) emission which strongly deviate from the well-known radio to FIR correlation (e.g., Condon 1992). Potential interpretations of the FIR excess include very young synchrotron-deficient starbursts or dust-enshrouded active galactic nuclei (AGNs). FIR-excess galaxies only represent a small sub-group (≈1%) of the IRAS Faint Galaxy Sample (e.g., Roussel et al. 2003), which is probably an indication that they may be tracing a short evolutionary phase. If powered by obscured AGN, these are likely to be in the early stages of their evolution, when the nuclear material has not yet been dispersed and/or consumed to feed the growth of the black hole. Recent publications (Aalto et al. 2012; Sakamoto et al. 2013; Aalto et al. 2016) have shown that some of such systems drive molecular outflows and are thus the ideal targets to study the first stages of starburst/AGN feedback.

The most extreme FIR-excess galaxy detected so far is NGC 1377, a lenticular galaxy in the Eridanus group at a distance of 21 Mpc (1″ = 102 pc), with a FIR luminosity of the order of 10^9 $L_\odot$ (Roussel et al. 2003). Despite several attempts in the past, the radio continuum in this galaxy has long remained undetected. Deep observations with the Very Large Array (VLA) and Effelsberg telescopes (e.g., Roussel et al. 2003, and references therein) obtained limits on the radio continuum which are about 40 times fainter than the synchrotron emission that would be expected from the radio to FIR correlation (Fig. 1). Also, these limits are fainter than the free-free emission that would be expected from the star formation rate (SFR) of 1−2 $M_\odot$ yr^{-1} derived from the IR flux. HII regions are not detected through near-infrared (MIR) hydrogen recombination lines or thermal radio continuum (Roussel et al. 2003, 2006). Deep mid-infrared (MIR) silicate absorption features suggest that the nucleus is very compact, and enshrouded by a large mass of dust (e.g., Spoon et al. 2007), which potentially absorbs all

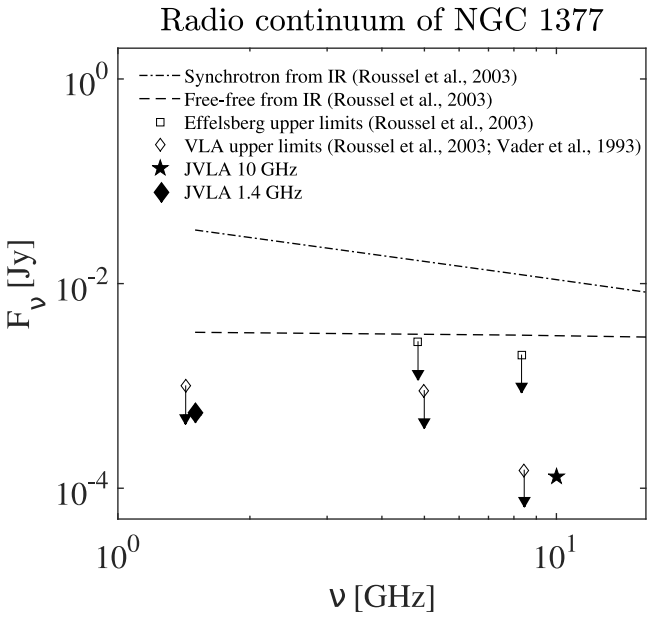

Fig. 1. Radio continuum flux of NCG 1377 compared to free-free and synchrotron emission expected from IR fluxes. Filled symbols refer to our detections of the radio continuum with the JVLA. The upper limits are 3σ estimates from the literature.

ionizing photons. The high obscuration makes the determination of the energy source a challenging task.

Roussel et al. (2006) proposed that NGC 1377 is a nascent opaque starburst – the radio synchrotron deficiency would then be caused by the extreme youth (pre-supernova stage) of the starburst activity when young stars are still embedded in their birth-clouds. In contrast, Imanishi (2006) argued, based on the small 3.3 μm PAH equivalent width and strong MIR H_2 emission, that NGC 1377 harbors a buried AGN. Furthermore, Imanishi et al. (2009) found an HCN/HCO^+ $J = 1-0$ line ratio exceeding unity, which they suggested is evidence of an X-ray dominated region (XDR) surrounding an AGN. The authors explained the lack of radio continuum by the presence of a large column of intervening material that causes free-free absorption.

With recent Submillimeter Array (SMA) and Atacama Large Millimeter/submillimeter Array (ALMA) observations, Aalto et al. (2012, 2016) found a molecular outflow originating from the inner 30 pc of NGC 1377 and extending to about 150−200 pc. Given its velocity and extent, these authors calculate an age for the outflow of about 1.4 Myr, which is consistent with the young age of the central activity. The authors find that the upper limit on the 1.4 GHz flux density is too low to explain the outflow as supernova-driven and suggest instead that it may be driven by radiation pressure from a buried AGN.

In summary, there is substantial evidence that the energy source of NGC 1377 must be young, but its nature is still highly debated. Here we report the results of recent observations with the Enhanced *Karl G. Jansky* Very Large Array (JVLA) and *Chandra* X-ray observatory which finally reveal the energy source of NGC 1377 and shed new light on the properties of FIR-excess galaxies. The details of the observations are reported in Sect. 2. In Sect. 3 we describe the properties of the radio and X-ray emission and compare the observations with synthetic starburst models. In Sect. 4 we discuss the nature of the nuclear energy source and in Sect. 5 we summarize our conclusions.

2. Observations and data reduction

2.1. Radio JVLA X-band

We observed NGC 1377 using the JVLA in C-configuration at *X*-band (8−12 GHz) in full polarization mode, under project 14B-120. The total bandwidth was 4 GHz, split into 32 spectral windows. The observations were performed in October 2014. The total on-source time was 1.8 h. We used 3C 138 for flux and bandwidth calibration, and J0340-2119 as the phase calibrator, at an angular distance of 1.0° from NGC 1377.

We used the Common Astronomy Software Applications package (CASA, McMullin et al. 2007) to perform a standard data reduction. We imaged the data using the multi-frequency synthesis (MFS) algorithm with a natural weighting and a pixel size of 0.4″. The synthesized beam size was 5.0″ × 2.2″, with a position angle (PA) of −26°. We achieved a rms noise level of 4 μJy/beam. The resulting map is shown in Fig. 2.

2.2. Radio JVLA L-band

L-band observations at 1.5 GHz were carried out in June 2015 (project 15A-501) with the JVLA in A-configuration, with a bandwidth of 1 GHz. The data reduction was analogous to our *X*-band data. We imaged the data using a cell size of 0.25″ and a synthesized beam size of 1.8″ × 1.1″, with a PA of 3°. The total on-source time was two hours.

The MFS imaging of the *L*-band data was complicated by the presence in the field of two strong radio sources: NVSS J033644-205849 located 5 arcmin to the south of NGC 1377 and with a peak flux density of 65 mJy beam^{-1}, and NVSS J033645-203637, 16 arcmin to the north, with 14 mJy beam^{-1}. This complication was twofold: first, the dynamic range of the image was limited, not being able to reach the nominal rms, and second, intense side-lobes appeared when we only imaged the area around NGC 1377. This was not problematic in the *X*-band observations because of the steep spectral index of the two bright sources. To minimize the side-lobes, we mapped a very large area (50 × 17 arcmin) to include both sources in the field of view (see Fig. 3). While at such angular distances, smearing effects appear, the side-lobes of the resulting image were significantly reduced. We finally performed several phase-only self-calibration rounds, to improve the calibration of the data, yielding to a local off-source rms of 10 μJy beam^{-1}. The resulting *L*-band continuum image is shown in Fig. 2, while a journal of the observations is reported in Table 1.

2.3. Chandra X-rays

Chandra observed NGC 1377 on 2013-12-10 for 49 ks with ACIS-S (ObsID: 16086). The data reduction was performed using the CIAO 4.7 software. To obtain an image and spectra, we followed the *Chandra* analysis guide[1] and first ran the `chandra_repro` script to produce cleaned *level = 2* event files.

The resulting image is shown in Fig. 4. No emission is detected at the known position of the center of NGC 1377, but a faint signal is present to the south-west, about 4.″5 from the center. To estimate the significance of this detection we integrated the X-ray emission in a circular aperture of 2″ centered at 3h36m38.93s, −20°54′10.9″. As background region we chose an annulus centered on the source position with an inner radius of 7″ and an outer radius of 14″. In the source region we detect five counts, which by applying Poisson statistics correspond to a

[1] http://cxc.harvard.edu/ciao/guides/#acis

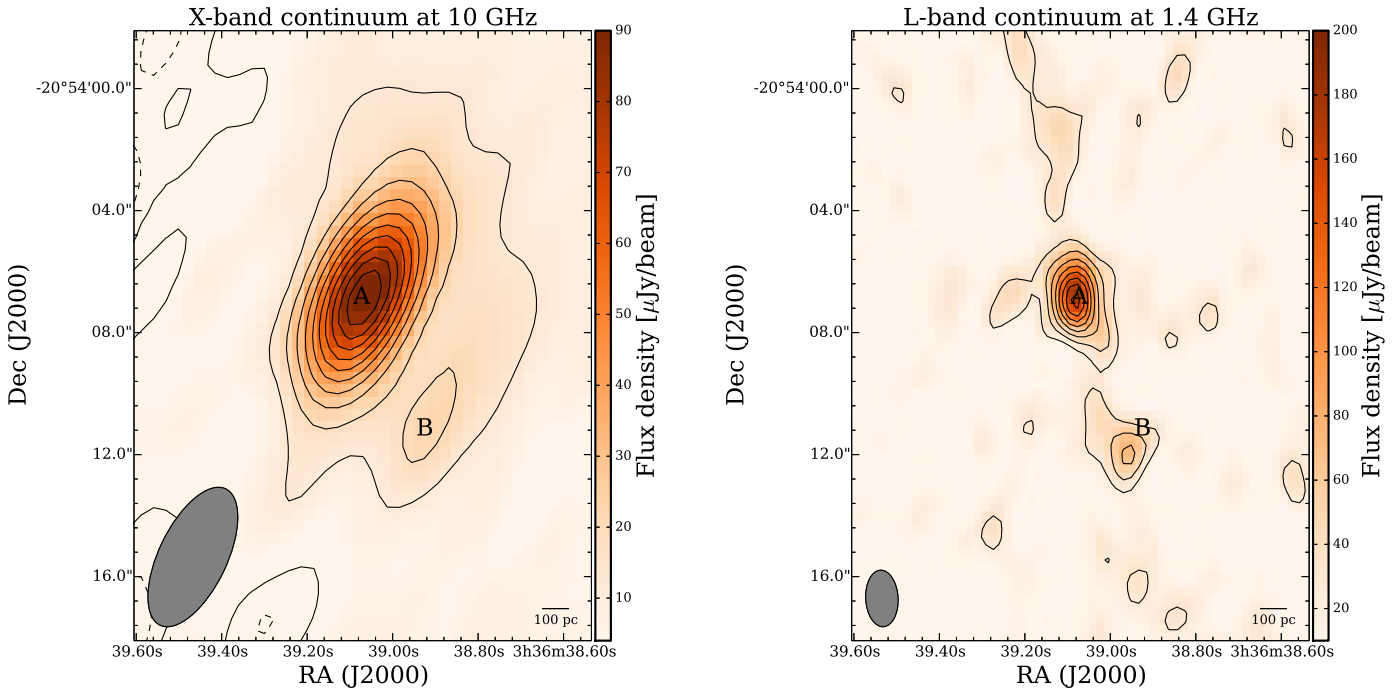

Fig. 2. Continuum emission maps at 10 GHz (*left*) and 1.5 GHz (*right*) obtained with the JVLA in NGC 1377. The solid contours are drawn every 2σ starting at 3σ. The rms noise is 4 μJy/beam and 13 μJy/beam in the *X*- and *L*-band image, respectively. Negative values are drawn as dashed contours. The two main emission components are labeled as *A* and *B*, see text for discussion.

Table 1. Journal of JVLA observations.

Frequency	Observation date	Configuration	Beam [maj (″) × min (″), PA (°)]	Noise rms [μJy/beam]	Peak flux density [μJy/beam]
X band (10 GHz)	October 2014	C	4.9 × 2.2 , −26	4	82
L band (1.4 GHz)	June 2015	A	1.8 × 1.1 , 3	10	178

signal-to-noise ratio of 2.2. This detection has thus to be considered as tentative. A similar analysis was performed for the faint emission around the galaxy center which has a signal-to-noise ratio lower than two and will be considered as a non-detection.

3. Results

3.1. Morphology of the radio continuum

The radio continuum of NGC 1377 is detected, for the first time, in both *X* and *L*-bands with peak flux densities of 82 ± 4 μJy/beam and 178 ± 13 μJy/beam, respectively. The maps in Fig. 2 show that in both bands the emission is distributed into two main components, labeled A and B. The A component contains most of the flux and is peaked on the center of the galaxy, while the B component is displaced to the south-west by 4.″5, corresponding to ∼500 pc at the galaxy's distance.

The B component is detected with a signal to noise ratio of seven in *X*-band and five in *L*-band, which makes it unlikely that the emission is completely caused by residual effects from the synthesized beam. We note however that the position of the peak of the B component is not exactly the same in the *L*- and *X*-band images, which may be due to a residual effect from the strong steep-spectrum source in the field of view of *L*-band observations (see Sect. 2.2). With the data at our disposal we cannot exclude the possibility that a fraction of the emission of the *L*-band B component is due to un-removed emission from such a strong radio source, which escaped the MFS cleaning.

To better characterize the structure of the radio emission we performed a 2D Gaussian fit with the CASA routine `imfit`. The results of the fit are shown in Table 2. In *X*-band, the A component has a flux density of 160 ± 12 μJy and is barely resolved, with a de-convolved size of 4.″4 × 2.″5, which is only slightly larger than the synthesized beam. The B component is best fit by a point source of flux density 25 ± 2 μJy. A similar result is found in *L*-band, where the A component is barely resolved, with a de-convolved size of 2.″6 × 1.″7 and a flux density of 427 ± 69 μJy. The B component in *L*-band is best fit by a point source of 101 ± 19 μJy.

3.2. Radio spectral index

Assuming the radio spectral energy distribution (SED) to be described by power law of the kind $S_\nu \propto \nu^{-\alpha}$, the Gaussian fit of Table 2 results in a spectral index $\alpha = 0.5 \pm 0.1$ for the A component and $\alpha = 0.7 \pm 0.2$ for the B component.

In order to produce a map of the radio spectral index in NGC 1377, a low-resolution *L*-band map was derived by smoothing the *L*-band clean image to the *X*-band resolution with the CASA task `imsmooth`. This allowed a pixel-to-pixel comparison of the intensities in the *X*- and *L*-band maps. The resulting spectral index map is shown in Fig. 5. The map shows a spectral index gradient, with α steepening to the south-west from a value of 0.6 at the A position to 0.7−0.8 for the B component.

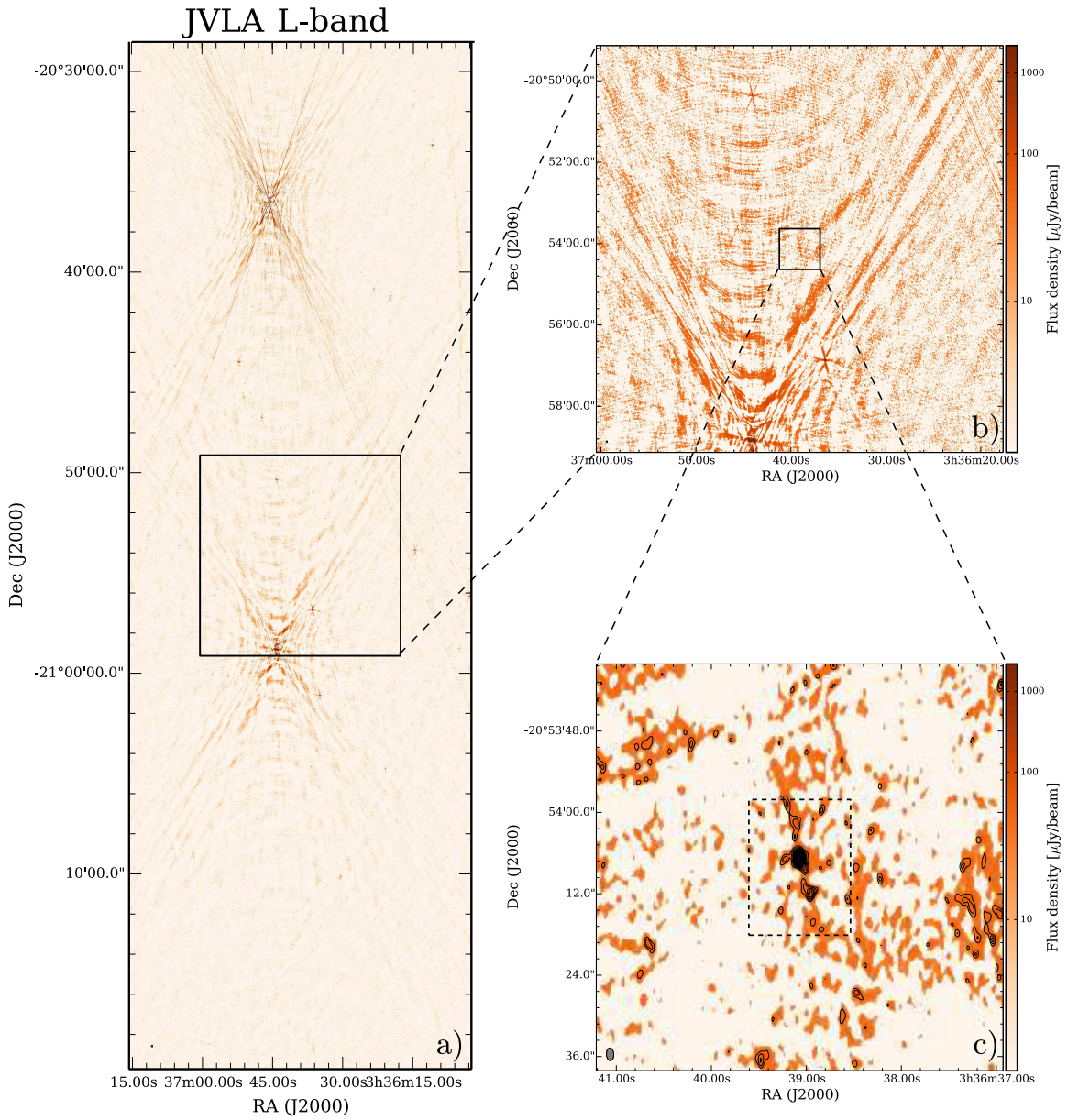

Fig. 3. **a)** Large-scale clean map of the JVLA *L*-band observations. The strongest source in the field is NVSS J033644-205849 (south of NGC 1377), with a peak flux of 64.7 mJy. The image has a dynamic range of 6470, with an rms of 10 μJy. **b)** $10' \times 10'$ region around NGC 1377 showing the main sources of contamination. **c)** $1' \times 1'$ region around NGC 1377. Contours are drawn every σ, starting at 3σ. The dashed rectangle marks the area shown in Figs. 2–10.

The spectral index derived for the B component is very close to the non-thermal spectral index observed in star forming galaxies and AGN radio jets, which is generally associated with optically thin synchrotron emission ($\alpha \simeq 0.7$–0.8, e.g. Condon 1992). However, because of a possible contribution of the dirty beam from the steep spectrum source in the *L*-band (see Sect. 2.2), the spectral index of 0.7 for the B component has to be considered as an upper limit.

3.3. Constraints on the free-free opacity

One of the possible explanations for the extreme radio deficiency of NGC 1377 has been proposed to be free-free absorption of the synchrotron emission from a compact starburst or AGN (e.g., Roussel et al. 2003; Imanishi et al. 2009). Our detection of the *X*- and *L*-band fluxes allow us to put some constraints on the free-free opacity and electron density in the galaxy.

If we assume the radio spectrum to be due to a synchrotron source and foreground thermal free free emission, we can write the total radio flux density as

$$S = S_{\rm NT}\, {\rm e}^{-\tau_{\rm T}} + S_{\rm T}\,(1 - {\rm e}^{-\tau_{\rm T}})\,, \tag{1}$$

where $S_{\rm NT}$ is the non-thermal synchrotron emission, $S_{\rm T}$ is the thermal free-free emission, and $\tau_{\rm T}$ is the free-free opacity. Following Condon (1992),

$$\tau_{\rm T} = 3.3 \times 10^{-7} \left(\frac{EM}{\rm cm^{-6}\ pc}\right) \left(\frac{T_{\rm e}}{10^4\ \rm K}\right)^{-1.35} \left(\frac{\nu}{\rm GHz}\right)^{-2.1}, \tag{2}$$

where $T_{\rm e}$ is the electron temperature and $EM = \int n_{\rm e}^2\, {\rm d}l$ is the emission measurement determined by the electron density $n_{\rm e}$ and

Table 2. Results of the Gaussian fit of the continuum components in *X*- and *L*-band with the CASA routine `imfit`.

Component	Position [RA (h:m:s) , Dec. (° :′:″)]	Deconvolved size [maj (″) × min (″), PA (°)]	Peak flux density [μJy/beam]	Flux density [μJy]
X-band A	3:36:39.06, −20:54:06.8	4.4 ± 0.7 × 2.5 ± 0.3, 163 ± 12	80 ± 4	160 ± 12
X-band B	3:36:38.93, −20:54:10.9	point source	28 ± 4	25 ± 2
L-band A	3:36:39.07, −20:54:06.8	2.6 ± 0.7 × 1.7 ± 0.6, 26 ± 68	179 ± 21	427 ± 69
L-Band B	3:36:38.96, −20:54:11.8	point source	101 ± 21	101 ± 19

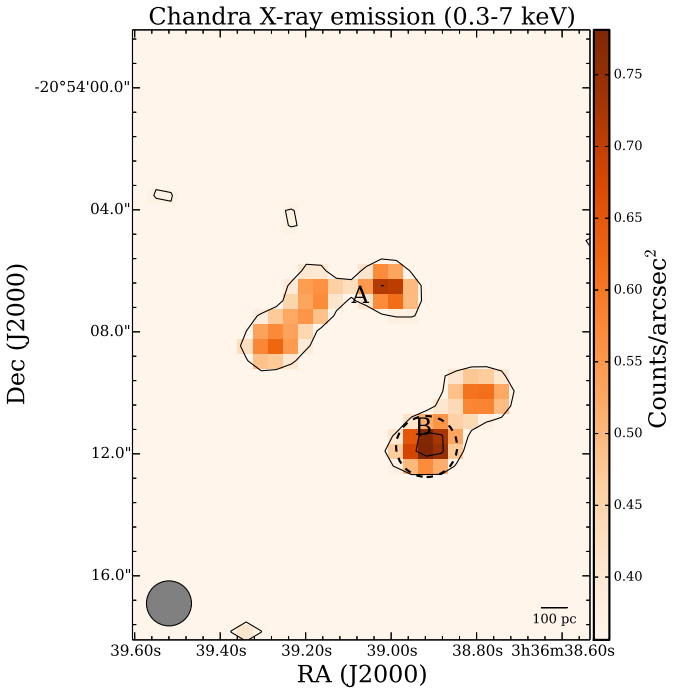

Fig. 4. Detection of X-rays emission with *Chandra*. The observations were smoothed to a resolution of 1.″5. Contours are drawn every 0.35 counts/arcsec^2 starting at 0.35 counts/arcsec^2. The galaxy center is marked as A. The dashed ellipse shows the 2″ × 2″ region around position B which was used to calculate a signal-to-noise of 2.2σ (see Sect. 2.3 for discussion).

the extent of the free-free absorber dl along the line of sight. In our case we assume a constant n_e in a spherical region with diameter of 2″ (∼230 pc), which is the angular size determined by the Gaussian fit of Table 2 for the A component. For the B component, the chosen value is an upper limit to the size of the emitting region.

We assume the thermal free-free emission to be a black body at temperature T_e in the Rayleigh–Jeans regime:

$$S_T = \Omega \frac{k_B T_e \nu^2}{c^2}, \quad (3)$$

with Ω the solid angle subtended by the source. For the non-thermal emission we assume a form $S = S_{NT} = F_{NT}\nu^{-\alpha_{NT}}$, with F_{NT} constant.

We assume an optically-thin synchrotron spectral index of $\alpha_{NT} = 0.8$ and an electron temperature $T_e = 10^4$ K, as in Condon (1992). At low opacities, the thermal part of Eq. (1) has only a very weak dependence on the electron temperature ($S_T\tau_T \propto T_e^{-0.35}$), so that an error of one order of magnitude in T_e would change the resulting free-free emission by only a factor of two. With our assumptions, the observed radio flux density only depends on the value of the non-thermal constant F_{NT} and on the electron density n_e, which can be determined by fitting Eq. (1) to the *L*- and *X*-band fluxes. The results of the χ^2-minimization fit are shown in Fig. 6, while the χ^2-surfaces are shown in Fig. 7.

For the A component we find that the emission is best fit by $EM \simeq 10^4$ cm^{-6} pc, corresponding to an electron density $n_e \simeq 7$ cm^{-3}. The free-free opacity is very low, of the order of 10^{-3} and 10^{-5} at 1.5 and 10 GHz, respectively. The free-free contribution to the total radio flux goes from 25% at 1.5 GHz to about 50% at 10 GHz. For the B component the fit results in an $EM < 10^3$ cm^{-6} pc, corresponding to an electron density $n_e <$ 2 cm^{-3}. The free-free opacity in both *L*- and *X*-band is found to be negligible, with values $<10^{-5}$. The free-free contribution to the total radio flux goes from 5% at 1.5 GHz to about 15% at 10 GHz.

These results should be considered as order-of-magnitude estimates because of the many assumptions of our analysis. The free-free contribution resulting from our fit depends on the assumed non-thermal spectral index, which in some cases (e.g., in AGN) could be lower than the standard $\alpha_{NT} = 0.8$. In our analysis, a shallower non-thermal spectral index would result in an even lower free-free emission. The estimated free-free contributions have thus to be considered as upper limits. The main uncertainty affecting the derived electron densities comes from the unknown size of the free-free emission region. For the A component the choice of a 2″ source is justified by our Gaussian fitting of Table 2 and partly by molecular gas observations. Aalto et al. (2012) found that the CO 2−1 emission is concentrated in the inner 200 pc of the galaxy and we can assume most of the free-free to be associated with star formation taking place in this molecular zone. However, it is unclear how much of the observed CO emission is associated with the molecular disk and how much is instead part of a molecular outflow. Recent results by Aalto et al. (2016) suggest that the launching region of the molecular outflow could be smaller than 30 pc and that the energy source should be located inside this region. A diameter of 30 pc for the radio source would imply an electron density $n_e \simeq 10^2$ cm^{-3}, corresponding to an *L*-band opacity $\tau_T = 0.08$.

3.4. The radio-infrared relation

One of the most used calibrations in extragalactic star-formation is the observed correlation of radio and infrared fluxes (e.g., Helou et al. 1985; Condon 1992; Yun et al. 2001), described by the factor

$$q_{IR} \equiv \log_{10}\left(\frac{L_{IR}}{3.75\times10^{12}L(1.4\ \mathrm{GHz})}\right). \quad (4)$$

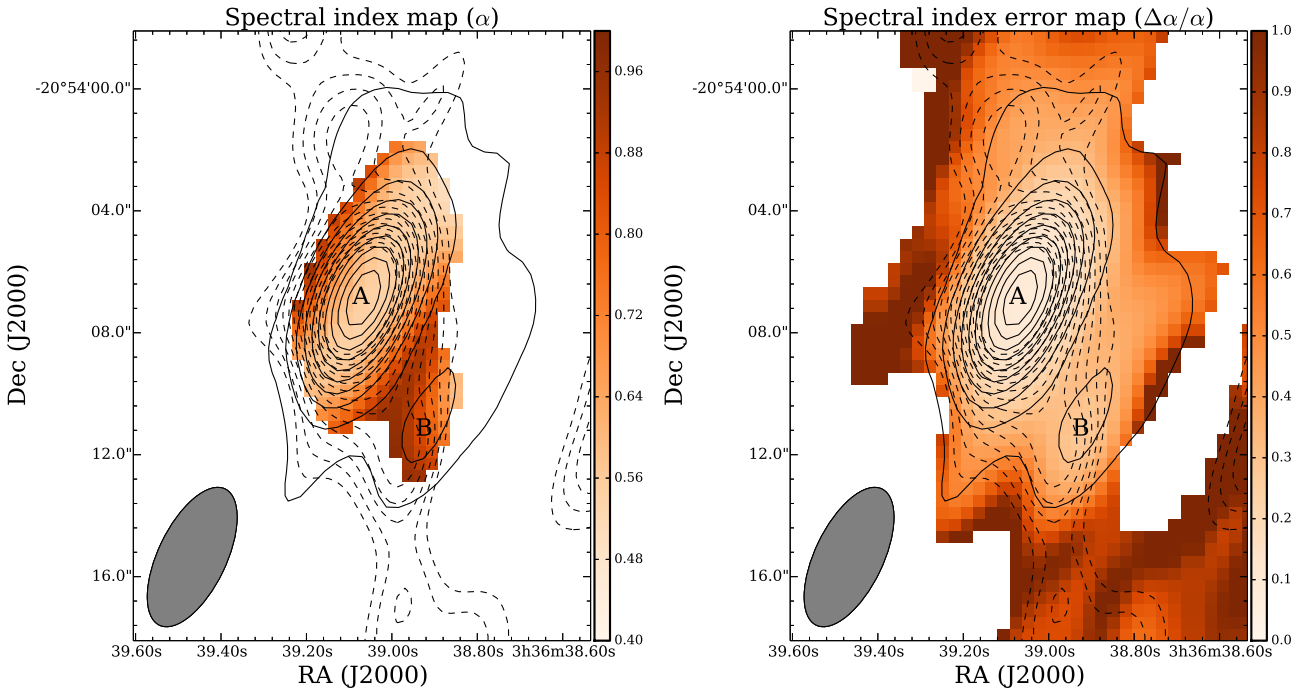

Fig. 5. *Left*: spectral index map for the radio emission in NGC 1377, derived from *X*- and *L*-band observations. Values are only shown where the spectral index uncertainty $\Delta\alpha/\alpha$ is less than 30%. Solid contours show the *X*-band emission and are the same as in Fig. 2. Dashed contours show the *L*-band continuum emission smoothed to the *X*-band resolution, see text for discussion. The two main emission components are labeled as A and B, as in Fig. 2. *Right*: map of relative uncertainty for the derived spectral index.

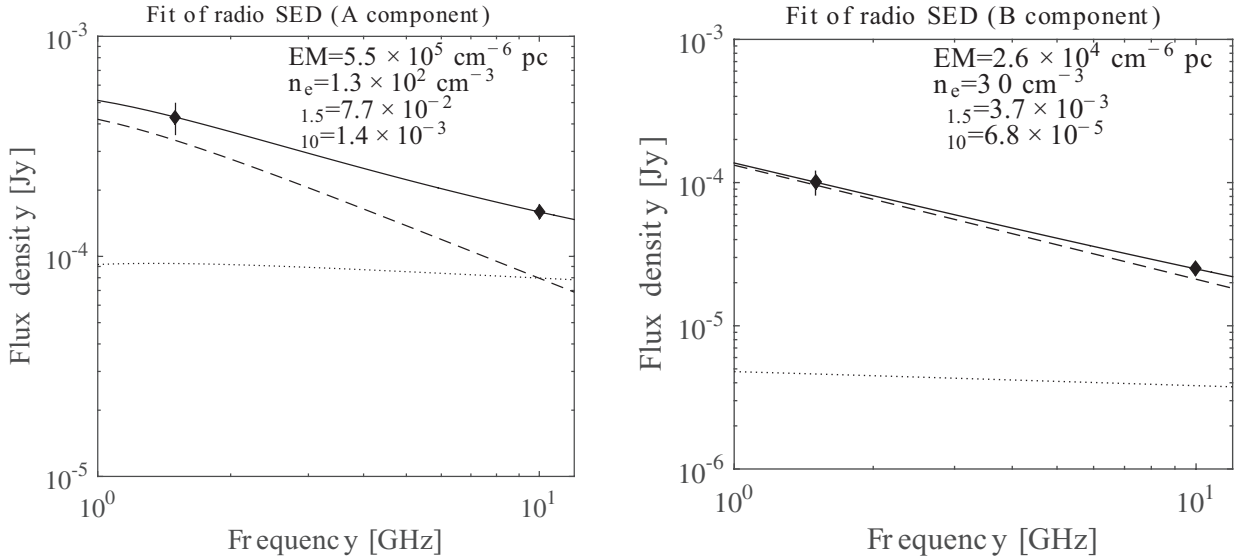

Fig. 6. Fit of the synchrotron and thermal free-free component of the radio emission of NGC 1377 for the A (*left*) and B (*right*) components. The measured flux density at *L*- and *X*-band is shown as filled diamonds. The total fit is shown as a solid line. The synchrotron and free-free components are drawn as a dashed and dotted line, respectively.

The observed $q_{\rm IR}$ varies from 2.34 ± 0.26 dex (Yun et al. 2001) to 2.64 ± 0.26 dex (Bell 2003), depending on whether $L_{\rm IR}$ is integrated over the FIR or whole IR range. The tight correlation observed for large samples of star-forming galaxies can be explained by both the IR and radio emission to be tracing massive star formation, the IR tracing heating of dust by the UV from young stars and the radio tracing synchrotron emission from supernova-remnants (e.g., Condon 1992). Only a few % of the galaxies in the IRAS 2 Jy sample (Yun et al. 2001) deviate significantly from the radio-IR correlation. Radio-excess galaxies are generally associated with radio-loud AGN, while IR-excess galaxies have been suggested to harbor either a compact young starburst or an heavily obscured AGN and their nature is still debated (e.g., Roussel et al. 2003, 2006; Costagliola et al. 2013).

For NGC 1377, Imanishi et al. (2009) find an IR luminosity of 4.8×10^{43} erg s^{-1} (1.2×10^{10} $L_\odot$) by integrating the IRAS fluxes from 12 μm to 100 μm. For the A component we find an *L*-band luminosity of 2.8×10^{26} erg s^{-1} Hz^{-1}, which, for Eq. (4), results in a $q_{\rm IR} \simeq 4.7$. This value is about 8σ above the mean value of 2.64 ± 0.26 found for most star-forming galaxies (e.g.,

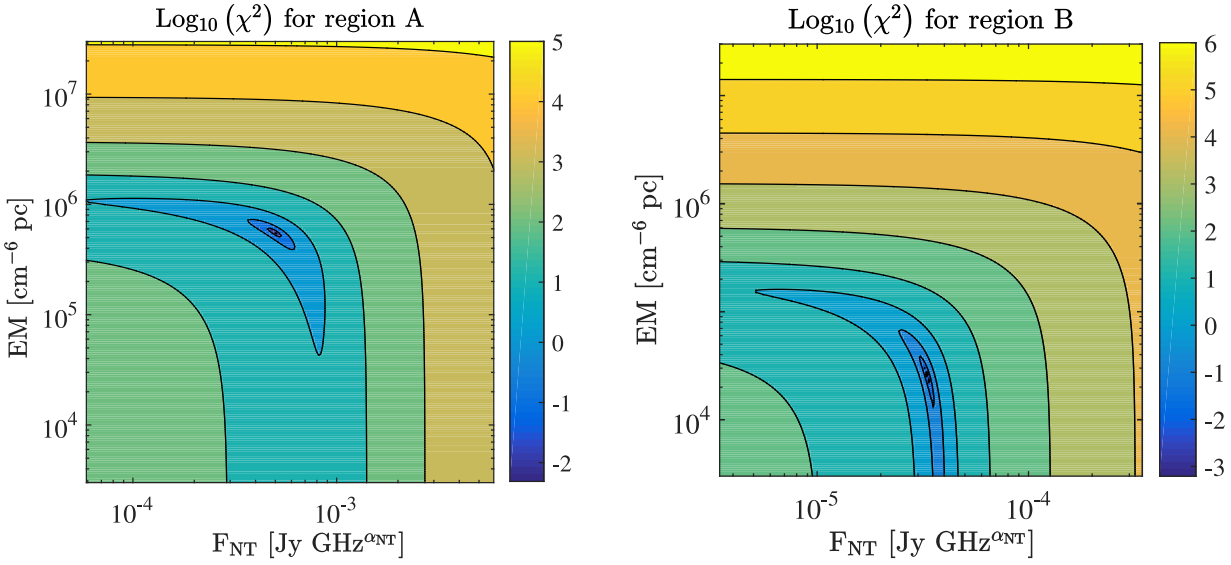

Fig. 7. χ^2 surfaces for the fit of the radio spectral energy distribution of the A (*left*) and B (*right*) components. The synchrotron constant is defined as $F_{\rm NT} \equiv S_{\rm NT}(1.5\ {\rm GHz})/1.5^{-\alpha_{\rm NT}}$, where $S_{\rm NT}(1.5\ {\rm GHz})$ is the synchrotron flux at 1.5 GHz and $\alpha_{\rm NT}$ is the non-thermal spectral index.

Bell 2003). A similar result is found when using the original definition of $q_{\rm FIR}$ by Helou et al. (1985) using the FIR flux. For a $L_{\rm FIR} = 4 \times 10^9\ L_\odot$ (Roussel et al. 2003) we find $q_{\rm FIR} = 4.2$, which deviates for more than 7σ from the mean value of 2.34 ± 0.26 found by Roussel et al. (2003). Our measurement confirms the extreme IR-excess of NGC 1377, which was first discussed by Roussel et al. (2003).

3.5. Star formation rate indicators

In this section we compare the SFR estimates derived from different diagnostics and briefly discuss the implications for the properties of star formation in NGC 1377. Most of these methods have been discussed by Murphy et al. (2011), and by Kennicutt & Evans (2012). The main results of our analysis are shown in Table 3.

Optical tracers: optical spectroscopic observations by Roussel et al. (2006) find no Hα emission in NGC 1377, but only weak NII and SII lines. These authors suggest that Hα emission from a nuclear starburst may be strongly attenuated by dust, as supported by the large opacity of the central IR source, and that NII and SII emission would be emerging from shocked low-ionization foreground gas. The large obscuration towards the nucleus thus makes it impossible to use standard optical SFR estimators.

Infrared tracers: radiation at infrared wavelengths can be used as a star formation tracer in highly obscured environments, assuming that most of the IR flux is generated by re-processed starlight. The emission at 24 μm is produced by absorption by dust of the UV light from young massive stars and is thus a good tracer of recent star formation. By using the calibration by Murphy et al. (2011) the 24 μm flux of NGC 1377 would correspond to a star formation rate of $SFR_{24\ \mu{\rm m}} = 2.6\ M_\odot\ {\rm yr}^{-1}$. A similar result is found for the SFR inferred from the total IR luminosity, $SFR_{\rm IR} = 1.9\ M_\odot\ {\rm yr}^{-1}$ (see Table 3, Eq. *h, i*).

Radio tracers: radio emission from star-forming galaxies is generally composed of optically thin synchrotron emission from electrons accelerated by SN explosions in the galactic magnetic field and by thermal free-free emission from the ionized gas around massive stars. The synchrotron flux is directly linked to the supernova rate and can be translated into a SFR by assuming an initial mass function (IMF, e.g., Condon 1992). For a Kroupa IMF (Kroupa 2001) the relation between non-thermal synchrotron flux and SFR found by Murphy et al. (2011) reads

$$SFR_{\rm NT} = 6.64 \times 10^{-29} \nu^{\alpha_{\rm NT}} L_{\rm NT}, \quad (5)$$

which for NGC 1377 results in a $SFR_{\rm NT} = 0.02\ M_\odot\ {\rm yr}^{-1}$.

The thermal free-free emission depends on the hydrogen ionization rate by UV photons from massive young stars, which for continuous star formation is proportional to the SFR. Murphy et al. (2011) find the following calibration

$$SFR_{\rm T} = 4.6 \times 10^{-28} \left(T_{\rm e}/10^4\ {\rm K}\right)^{-0.45} \nu^{0.1} L_{\rm T}, \quad (6)$$

where $T_{\rm e} \simeq 10^4$ K is the electron temperature and $L_{\rm T}$ is the thermal free-free luminosity in erg s^{-1} Hz^{-1}. Our best estimate of the thermal luminosity comes from the fit in Sect. 3.3 of the radio continuum for the A component, giving $L_{\rm T}(1.5\ {\rm GHz}) = 7.1 \times 10^{25}$ erg s^{-1} Hz^{-1}. Equation (6) then results in a $SFR_{\rm T} = 0.03\ M_\odot\ {\rm yr}^{-1}$, which is similar to that found from the non-thermal component.

Schmidt-Kennicutt relation: a correlation of the form $\Sigma_{\rm SFR} \propto \Sigma_{\rm gas}^{\alpha_{\rm SK}}$ between the surface gas density and SFR density in the disks of galaxies is observed throughout the Universe and is often referred to as the Schmidt-Kennicutt (SK) relation (e.g., Kennicutt & Evans 2012). The exponent $\alpha_{\rm SK}$ varies in the range 1−1.5, depending on the gas tracer used and on the galaxy type (e.g., Genzel et al. 2010; Daddi et al. 2010), but for local spirals the star formation and molecular gas surface densities are well described by the relation found by Kennicutt (1998)

$$\Sigma_{\rm SFR} = (2.5 \pm 0.7) \times 10^{-4} \Sigma_{\rm gas}^{1.4 \pm 0.15}\ M_\odot\ {\rm yr}^{-1}\ {\rm kpc}^{-2}, \quad (7)$$

where $\Sigma_{\rm gas}$ is the molecular gas surface density in $M_\odot\ {\rm pc}^{-2}$.

Interferometric observations of CO emission with the SMA (Aalto et al. 2012) and ALMA (Aalto et al. 2016) find that the molecular gas is concentrated in the inner 200 pc of the galaxy in a disk-outflow system (see Fig. 10). The dynamical mass of the inner 60 pc molecular disk is $4 \times 10^7\ M_\odot$, corresponding to a gas surface density of $\Sigma_{\rm gas} = 1.4 \times 10^4\ M_\odot\ {\rm pc}^{-2}$. The correlation of Eq. (7) would predict a SFR density of

Table 3. Multi-wavelength estimates of the SFR in NGC 1377.

$L_{\rm NT}$(1.5 GHz)[a]	2.8×10^{26} erg s^{-1} Hz^{-1}	[f] $SFR_{\rm NT} = 6.64 \times 10^{-29} \nu^{\alpha_{\rm NT}} L_{\rm NT}$ =	0.02 $M_\odot$ yr^{-1}
$L_{\rm T}$(1.5 GHz)[b]	7.1×10^{25} erg s^{-1} Hz^{-1}	[g] $SFR_{\rm T} = 4.6 \times 10^{-28} \left(T_{\rm e}/10^4\ {\rm K}\right)^{-0.45} \nu^{0.1} L_{\rm T}$=	0.03 $M_\odot$ yr^{-1}
$L(24\ \mu{\rm m})$[c]	1.2×10^{30} erg s^{-1} Hz^{-1}	[h] $SFR_{24\ \mu{\rm m}} = 5.58 \times 10^{-36} (\nu {\rm L}(24\ \mu{\rm m}))^{0.826}$=	2.6 $M_\odot$ yr^{-1}
$L_{\rm IR}$[d]	4.8×10^{43} erg s^{-1}	[i] $SFR_{\rm IR} = 3.88 \times 10^{-44} L_{\rm IR}$=	1.9 $M_\odot$ yr^{-1}
$\Sigma_{\rm gas}$[e]	$1.4 \times 10^4\ M_\odot$ pc^{-2}	[k] $SFR_{\rm SK} = 2.5 \times 10^{-4} \Sigma_{\rm gas}^{1.4} \times \pi\,(d/2)^2$=	0.45 $M_\odot$ yr^{-1}

Notes. [(a)] Radio luminosity at 1.5 GHz. [(b)] Thermal radio luminosity at 1.5 GHz from the fit of Sect. 3.3. [(c)] Luminosity at 24 μm, from Temi et al. (2009). [(d)] Total infrared luminosity from IRAS fluxes (Imanishi et al. 2009). [(e)] Molecular gas surface density from (Aalto et al. 2012) assuming a size of 200 pc. [(f)] SFR from non-thermal radio emission, Eq. (14) in Murphy et al. (2011). [(g)] SFR from thermal radio emission, Eq. (11) in Murphy et al. (2011). [(h)] SFR from 24 μm emission, Eq. (5) in Murphy et al. (2011). [(i)] SFR estimate from IR luminosity, Eq. (4) in Murphy et al. (2011). [(k)] SFR from molecular gas surface density, assuming a Schmidt-Kennicutt law with exponent 1.4 and a disk diameter d = 60 kpc.

$\Sigma_{\rm SFR} \simeq 160\ M_\odot$ yr^{-1} kpc^{-2}, corresponding to a $SFR_{\rm SK} = 0.45 \pm 0.12\ M_\odot$ yr^{-1} integrated over the molecular disk (Eq. k in Table 3).

3.6. Starburst99 models

The star-formation rate estimators discussed in Sect. 3.5 are summarized in Table 3. Because of the large uncertainties affecting these measurements (e.g., Kennicutt & Evans 2012) the SFR found have to be considered as order-of-magnitude estimates. Nevertheless, a significant scatter is evident, with IR diagnostics resulting in SFR more than two orders of magnitude greater than those estimated from our radio continuum observations. The most used SFR calibrators assume a continuous star formation and starburst ages greater than 100 Myr (e.g., Murphy et al. 2011). The observed discrepancy may be thus due to a time evolution of the observable properties of the star-forming region.

In previous studies, when only upper limits to the radio continuum of NGC 1377 were known, the extreme radio deficiency of NGC 1377 has been interpreted as the evidence of a nascent, pre-supernova starburst (e.g., Roussel et al. 2006). Synchrotron emission from supernovae is only produced a few Myr after the onset of the star-forming event, because massive stars need time to explode into supernovae and accelerate relativistic electrons through the magnetic field of the galaxy. Also, in a high-density dusty starburst HII regions around massive stars would be very compact and the ionizing UV would be absorbed by the high dust column, producing weak nebular emission in the optical.

To test whether the radio deficiency of NGC 1377 can be explained by a young opaque starburst, we compare some of the observed properties with synthetic starburst models obtained with the on-line version of `Starburst99`[2] (Leitherer et al. 1999). We run two sets of models assuming a continuous SFR varying from 0.01 to 10 $M_\odot$ yr^{-1} and an instantaneous star formation event with total stellar mass between 10^4 and 10^8 $M_\odot$. In all models we assume a standard Kroupa initial mass function with exponent 1.3 from 0.1 to 0.5 $M_\odot$ and 2.3 from 0.5 to 100 $M_\odot$. Infrared and mm-wave observations do not show any evidence of a low metallicity for NCG 1377 (e.g., Roussel et al. 2006) and in our models we consider $Z = Z_\odot$.

3.6.1. Non-thermal radio emission

The synchrotron emission from supernovae for the `Starburst99` models is shown in Fig. 8a. To derive the synchrotron luminosity from the supernova rate SNR we use the conversion $L_{\rm NT} = 13 \times 10^{29} \nu^{-\alpha_{\rm NT}}$SNR from Condon (1992), with ν in GHz and $\alpha_{\rm NT} = 0.8$. As expected, the synchrotron luminosity at 1.4 GHz is zero at times earlier than 3 Myr because no supernova has exploded yet, and in the continuous star formation case it then increases to a roughly constant value at $t > 100$ Myr. The shaded area in Fig. 8a shows the confidence interval of the L-band luminosity derived from our JVLA observations for the A component, $L_{\rm NT} = 2.8 \pm 0.5 \times 10^{26}$ erg s^{-1}. We see that the observed value is consistent with either a young starburst with age <10 Myr, or with an older system with $SFR \simeq 10^{-2}\ M_\odot$ yr^{-1}. An instantaneous starburst with total stellar mass between 10^5 and 10^6 $M_\odot$ and age between 10^6 and 10^7 could also explain the observed synchrotron flux.

3.6.2. Ionizing radiation

Free-free emission is produced by HII regions around young massive stars before they explode into supernovae and it is thus a better tracer of the early stages of the starburst compared to synchrotron radiation. Also, free-free radiation is a good tracer of young star formation in obscured environments because it is not affected by dust obscuration or, in the limit of optically-thin omission, by the compactness of the HII regions as is the case for other tracers such as Hα (e.g., Murphy et al. 2011).

For optically-thin free-free emission, the thermal radio luminosity is proportional to the production rate $N_{\rm UV}$ of Lyman continuum photons from HII regions around young massive stars. Following Condon (1992), we can write

$$N_{\rm UV} \geq 6.3 \times 10^{52} \left(\frac{T_{\rm e}}{10^4\ {\rm K}}\right)^{-0.45} \left(\frac{\nu}{\rm GHz}\right)^{0.1} \left(\frac{L_{\rm T}}{\rm W\ Hz^{-1}}\right), \quad (8)$$

where the inequality accounts for possible absorption of ionizing radiation by dust. Our estimate of the thermal free-free emission for the A component (see Sect. 3.3) results in a thermal radio luminosity at 10 GHz of $L_{\rm T} \simeq 6 \times 10^{18}$ W Hz^{-1}, which when substituted in Eq. (8) gives an ionizing photon production rate of $N_{\rm UV} \simeq 5 \times 10^{51}$ s^{-1}.

In Fig. 8b the $N_{\rm UV}$ derived from our observations is compared to the results of `Starburst99` models . The red shaded area shows the observed value, allowing for an uncertainty of 50%. In the models assuming continuous star formation, $N_{\rm UV}$ increases by one order of magnitude from 1 to 10 Myr and is proportional to the SFR. The observed value is consistent either with a young star-formation event with age <5 Myr and $SFR \simeq 0.1\ M_\odot$ yr^{-1} or with an older system with SFR of a few $10^{-2}\ M_\odot$ yr^{-1}.

[2] http://www.stsci.edu/science/starburst99/

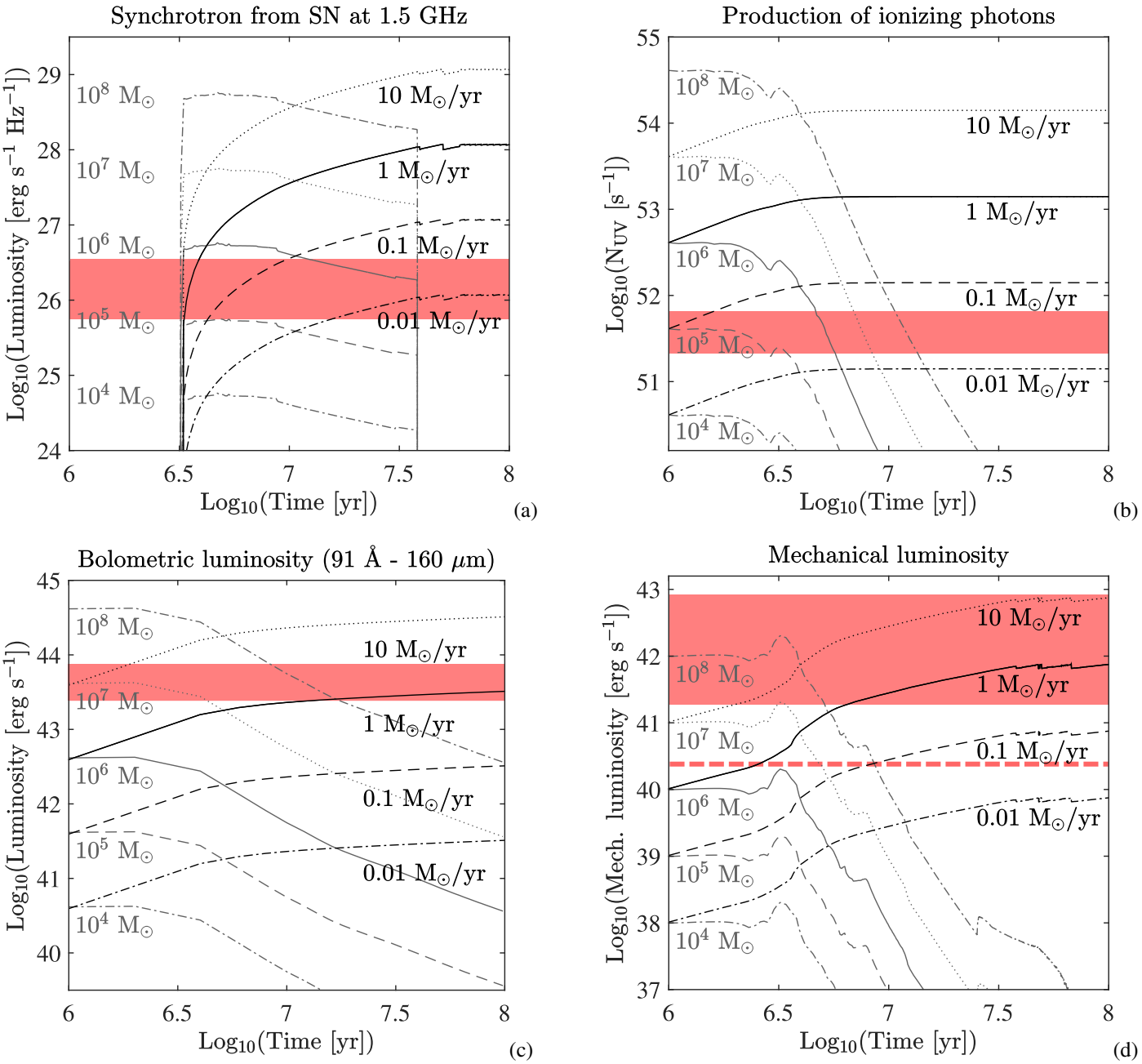

Fig. 8. Comparison of observed properties of NGC 1377 with `Starburst99` models. Black lines show results for models with continuous SFRs of 0.01, 0.1, 1, and 10 $M_\odot$/yr. Gray lines show results for models assuming instantaneous star formation with total stellar masses ranging from 10^4 to 10^8 $M_\odot$. **a)** Comparison of the observed X-band emission with the expected synchrotron emission at 1.5 GHz from supernovae. The shaded area shows the confidence interval of our measurement of the radio luminosity at 1.5 GHz. **b)** Production rate of ionizing photons ($N_{\rm UV}$) from HII regions. The shaded area shows the confidence interval for $N_{\rm UV}$ derived from our estimate of the thermal radio emission. **c)** Bolometric luminosity derived by integrating the continuum flux from the `Starburst99` models between 91 Å and 160 μm. The shaded area shows the IR luminosity derived by the IRAS fluxes (Imanishi et al. 2009) assuming a confidence interval of 50%. **d)** Mechanical luminosity from stellar winds and supernova explosions. The shaded area shows the confidence interval of the measurement of mechanical luminosity of the molecular outflow detected by Aalto et al. (2016) with ALMA in the CO J = 3–2 transition, assuming a Galactic CO-H_2 conversion factor (*massive jet*). The red dashed line shows the lower limit of the outflow mechanical luminosity assuming a conversion factor 10 times lower (*light jet*). See Sect. 3.6 for discussion.

For the models assuming instantaneous star formation, $N_{\rm UV}$ is roughly constant for the first 2 Myr and then decreases steeply as the massive stars responsible for most of the ionizing UV radiation explode into supernovae. If we assume an age of less than 3 Myr, the observed free-free emission constrains the total stellar mass to $\sim 10^5$ $M_\odot$. For an older instantaneous starburst the observed value is consistent with ages between a few 10^6 and a few 10^7 Myr for a total stellar mass range of 10^6–10^8 $M_\odot$.

3.6.3. Bolometric luminosity

In an opaque starburst, most of the optical and UV stellar radiation is absorbed by dust and re-radiated as thermal continuum in the infrared. In this scenario, the infrared luminosity is a good estimate of the bolometric luminosity of a starburst.

In Fig. 8c we compare the bolometric luminosity of the `Starburst99` models with the observed infrared luminosity of

NGC 1377. The bolometric luminosity was obtained by integrating the synthetic spectra from 91 Å to 160 μm. The total infrared luminosity of NGC 1377 derived from IRAS fluxes (Imanishi et al. 2009) is 1.2×10^{10} $L_\odot$.

For the models assuming continuous star formation, we find that the total IR luminosity is consistent with a young (<3 Myr) starburst with $SFR \approx 10$ $M_\odot$ yr^{-1}, or with a more evolved (>10 Myr) starburst with $SFR \approx 1$ $M_\odot$ yr^{-1}. In the case of instantaneous star formation, the bolometric luminosity is dominated by emission by massive stars and declines rapidly after ~3 Myr. For these models, the IR luminosity is consistent with a starburst with mass higher than 10^7 $M_\odot$ and age older than 1 Myr, increasing with total stellar mass.

3.6.4. Mechanical luminosity

Recent ALMA observations of CO $J = 3$–2 by Aalto et al. (2016) reveal a collimated bipolar outflow of molecular gas extending to more than 200 pc above the galactic plane. The de-projected outflow velocity estimates vary between 240 and 850 km s^{-1} depending on the assumed inclination, with an estimated upper limit to the H_2 mass of 10^7 $M_\odot$. This estimate is based on the CO luminosity assuming a standard CO-H_2 conversion factor, which may not be applicable to the gas in the outflow. If the gas is turbulent, the conversion factor may be an order of magnitude lower (e.g., Dahmen et al. 1998), which would imply an outflow mass as low as 10^6 $M_\odot$. Depending on the assumed conversion factor, the mass outflow rate may vary from 1–4 $M_\odot$ yr^{-1} for a *light* jet ($M(H_2) = 10^6$ $M_\odot$) to 10–40 $M_\odot$ yr^{-1} for a *massive jet* ($M(H_2) = 10^7$ $M_\odot$).

The mechanical luminosity of the outflow can be estimated as

$$L_{\rm mech} = \frac{1}{2}\frac{{\rm d}M}{{\rm d}t}V_{\rm out}^2, \quad (9)$$

which results in $L_{\rm mech} = 2 \times 10^{40}$–$9 \times 10^{41}$ erg s^{-1} for the *light jet* and 10 times higher for the *massive jet*.

In Fig. 8d we compare the mechanical luminosity of the observed molecular outflow with the mechanical luminosity from supernova explosions and stellar winds in the `Starburst99` models. In the case of continuous star formation, we find that in order to produce the observed mechanical luminosity the central starburst should have a SFR of more than 1 $M_\odot$ yr^{-1} and an age of more than 5 Myr. In particular we find that a pre-supernova starburst cannot drive the observed molecular outflow unless we consider extremely high SFR of a few 10 $M_\odot$ yr^{-1}. In the case of instantaneous star formation, we find that the observed mechanical luminosity could be reproduced by a young starburst of total stellar mass ~10^8 $M_\odot$ and age <2 Myr.

In the case of a *light jet*, that is, assuming a CO-H_2 conversion factor 10 times lower than the Galactic value, we find that the outflow energetics could be explained by a >5 Myr starburst with continuous $SFR > 0.1$ $M_\odot$ yr^{-1}, or by a young (<5 Myr) starburst with $SFR > 1$ $M_\odot$ yr^{-1}.

This comparison assumes a perfect coupling between the molecular gas and stellar feedback, that is, that all the mechanical energy produced by the starburst goes into driving the outflow. Such an assumption is probably not physical and we can expect only a fraction of the mechanical energy from the starburst to be transferred to the molecular outflow. This means that the values derived for the SFR or total stellar mass necessary to drive the outflow should be regarded as lower limits.

Table 4. Estimated X-ray luminosities of the B component assuming different hydrogen column densities. See Sect. 3.7 for discussion.

$N_{\rm H}$	L_{2-10} in erg s^{-1}
10^{24} cm^{-2}	5.7×10^{39}–5.1×10^{40}
10^{23} cm^{-2}	2.2×10^{38}–2.0×10^{39}
Galactic	1.7×10^{37}–1.5×10^{38}

3.7. First X-rays detection ?

Although no X-ray source is detected at the position of the NGC 1377 nucleus (Sect. 2.3), we tentatively detect X-ray emission 4.″5 to the south-west, with a signal to noise ratio of 2.2 in the 0.3–7 keV band. The position of the X-ray source (*Chandra*'s astrometric accuracy is 0.8″) coincides with the position of the radio peak B.

The signal-to-noise ratio of the X-ray spectrum is insufficient to accurately constrain the spectral shape, but by assuming a spectral model we can deduce the intrinsic X-ray flux. To obtain a flux estimate, an absorbed power law spectrum with a photon index of 1.9, such as is seen for a jet hot-spot (Hardcastle et al. 2016) is fitted to the data. The obtained intrinsic luminosity estimates at the 90% confidence limit in the 2–10 keV band for different columns are given in Table 4. We find that the intrinsic X-ray luminosity of the B component varies from 10^{38} to 10^{40} erg s^{-1} for assumed column densities of 10^{23}–10^{24} cm^{-2}.

4. Discussion

4.1. A nascent starburst ?

The extremely high IR/radio ratio of NGC 1377 has been interpreted as the signature of a pre-supernova opaque starburst (Roussel et al. 2003, 2006). This interpretation was mainly based on the non-detection of the radio continuum by VLA and Effelsberg observations (see Fig. 1). In this scenario the low Hα flux would be due to the extreme obscuration by dust, as revealed by deep MIR silicate absorption (e.g., Spoon et al. 2007), and by the high pressure which would limit the growth of HII regions.

Our JVLA observations reveal a steep radio spectral index in the nucleus of NGC 1377, which is usually associated to non-thermal synchrotron emission. In a pre-supernova starburst, the dominant emission mechanism should be thermal free-free from HII regions which would result in a flatter spectrum. This is exemplified by Fig. 9, where we show the evolution of the radio spectral index with starburst age derived from the `Starburst99` models of Sect. 3.6. The observed radio spectral index of 0.5 ± 0.1 is not consistent with a pre-supernova starburst.

The `Starburst99` models of Sect. 3.6 show that in order to be consistent with the observed IR luminosity, an obscured starburst of age <10 Myr should have a SFR higher than 2 $M_\odot$ yr^{-1}, or an instantaneous stellar mass greater than 10^7 $M_\odot$ (see Fig. 8c). The synchrotron flux derived by our JVLA observations is consistent with a young starburst mainly because around the threshold for supernova explosion (at about 3 Myr) the models are highly degenerate in SFR (see Fig. 8a). A more precise indication of the properties of the putative nascent starburst is given by our estimate of the ionizing photon flux from the observed free-free emission in Fig. 8b, which shows that a nascent starburst of age <10 Myr should have a $SFR < 0.1$ $M_\odot$ yr^{-1}, or an instantaneous stellar mass lower that 10^6 $M_\odot$ in order to be consistent with the observations. The

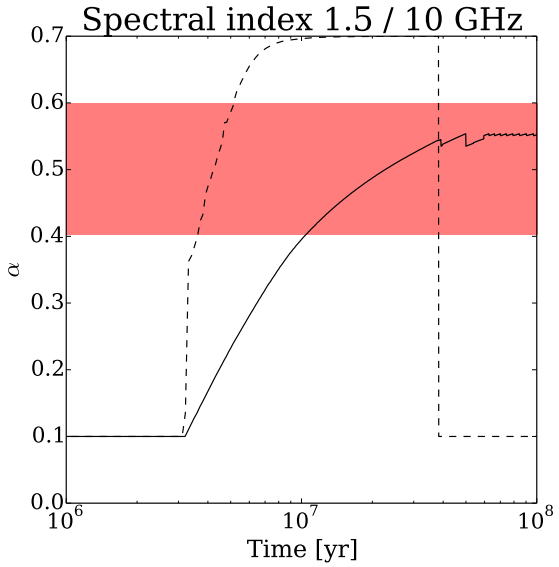

Fig. 9. Evolution of the 1.5−10 GHz spectral index from `Starburst99` models (see Sects. 3.6.1 and 3.6.2). The solid and dashed lines represent respectively continuous and instantaneous star formation models. The shaded area shows the confidence interval of the spectral index derived for the NGC 1377 nucleus.

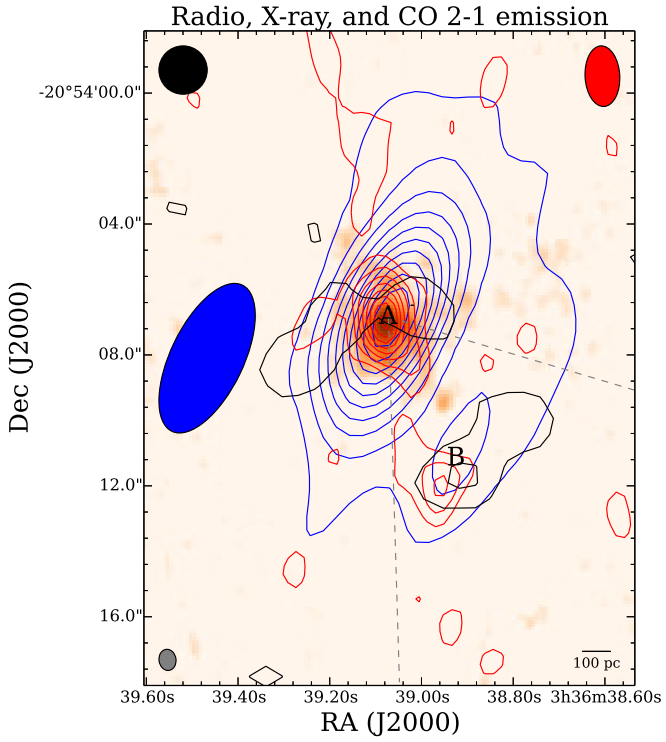

Fig. 10. Map of radio, CO and X-ray emission in NGC 1377. The radio continuum emission at L (left) band is shown as blue contours, the beam is shown in blue. The radio continuum emission at X (left) band is shown as red contours, the beam is shown in red. The moment 0 map of CO $J = 2-1$ emission from Aalto et al. (2012) is shown in color, the beam is shown in gray. The X-rays flux is shown in black contours, *Chandra* smoothed beam is shown in black. The gray dashed lines show the opening angle of the blue-shifted component of the molecular outflow cone detected in CO by Aalto et al. (2012).

upper limit to the SFR of the nascent starburst is more than one order of magnitude lower than the SFR derived from the IR luminosity. The discrepancy remains in the case of instantaneous star formation, with the radio and IR observations resulting in stellar masses which differ by more than one order of magnitude.

Also, the nascent starburst scenario cannot explain the energetics of the massive molecular outflow observed in CO (Aalto et al. 2012, 2016). In order to be explained by stellar winds or momentum injection by supernova explosions, the mechanical luminosity of the outflow would require a SFR of 1−10 $M_\odot$ yr^{-1} or an instantaneous starburst mass of 10^7−10^8 $M_\odot$, which are one to two orders of magnitude higher than the values estimated from the radio free-free luminosity. Moreover, Starburst-driven outflows are generally wide-angle winds and it is not clear how they could create a highly collimated molecular jet like the one observed in CO 3−2. Therefore, the nascent starburst scenario cannot explain all the observed properties of the central 200 pc of NGC 1377.

4.2. An obscured AGN ?

The presence of a non-stellar energy source in NGC 1377 was already suggested by Imanishi (2006) to explain the small observed PAH equivalent width at 3.3 μm. In addition, the HCN/HCO$^+$ $J = 1-0$ line ratio exceeds unity, which Imanishi et al. (2009) interpreted as evidence of an X-ray dominated region (XDR) surrounding an AGN. However, the most convincing evidence came with the detection of the CO molecular outflow by Aalto et al. (2012), who calculated that the upper limit on the 1.4 GHz flux density fell short by a factor of ten to explain the outflow as supernova-driven and suggested instead that the outflow may be driven by radiation pressure from a buried AGN. From the calibration of the stellar velocity dispersion and black hole mass (e.g., Graham et al. 2011), Aalto et al. (2012) derive a supermassive black hole (SMBH) mass of about 1.5×10^6 $M_\odot$. If the IR luminosity of NGC 1377 is produced by accretion onto the SMBH, this should be operating at more than 20% of its Eddington limit, placing it in the *quasar accretion* mode (e.g., Croton et al. 2006; Janssen et al. 2012; McAlpine et al. 2015).

When the presence of an AGN was first suggested by Imanishi (2006), the authors explained the lack of radio emission by a high free-free opacity due to the compact circumnuclear starburst. However, our fit of the radio continuum at *L*- and *X*-band finds very low free-free optical depths and a steep spectral index of $\alpha \simeq 0.5-0.6$, which are not consistent with a free-free absorbed radio-loud AGN. If an AGN is hiding at the core of NGC 1377 it must be extremely radio faint. The contribution of radio emission to the luminosity of an AGN is often expressed with the radio-loudness parameter $R \equiv L_{5\mathrm{GHz}}/L_{4400\ \text{Å}}$. A well established observational result is that optical quasars show a bimodal distribution around $R = 10$, with the majority of them being radio-quiet, with $0.1 > R > 1$ (e.g., Kellermann et al. 1989). By comparing the optical B band flux density of NGC 1377 (0.012 Jy, Dale et al. 2007) with the flux density at 5 GHz (interpolated from our *L*-band measurement assuming a spectral index $\alpha = -0.5$) we find $R = 0.02$, which defines the galaxy as an extremely radio faint source. A well defined anti-correlation between R and the Eddington ratio $\epsilon \equiv L_{\mathrm{Bol}}/L_{\mathrm{Edd}}$ is observed (e.g., Sikora et al. 2007). For NGC 1377, the correlation of Fig. 3 by Sikora et al. (2007) would predict an Eddington ratio of about unity, which is consistent with the high ϵ needed to drive the observed outflow and IR luminosity.

Table 5. Detectability of a black hole with $M_{BH} = 1 \times 10^6\ M_\odot$ in a *Chandra* ACIS observation with 44 ks net exposure.

N_H	L/L_{edd}	0.05	0.1	0.5	1.0
10^{24} cm^{-2}		D	D	D	D
10^{25} cm^{-2}		ND	ND	ND	ND

Notes. The results are shown in dependence of Eddington ratio and column density. D indicates a detection at a signal-to-noise of 2 or greater in the whole *Chandra* band and ND indicates a non-detection.

We further tested if a $10^6\ M_\odot$ black hole accreting at the Eddington limit is consistent with the non-detection of the nucleus of NGC 1377 in the X-ray band. We performed spectral simulations based on our *Chandra* observation, utilizing the spectrum extracted from the center as a basis, i.e. ensuring that the simulated spectra have the same exposure and same background properties as the actual exposure. The assumed spectral model is an absorbed power law with a photon index of 1.9 with the appropriate normalization for different Eddington ratios ($L/L_{edd} = 0.05, 0.1, 0.5, 1.0$). To obtain the theoretical 2−10 keV fluxes for a given Eddington ratio, we used Bolometric corrections from Vasudevan & Fabian (2007; $\lambda_{2-10} = 15, 20, 50, 60$). The spectra were then simulated using the command `fakeit` in the X-ray spectral modeling software `xspec` (Arnaud 1996). We find that a column of 10^{25} cm^{-2} is required to bring an AGN accreting at the Eddington limit into agreement with our *Chandra* non-detection (see Table 5). This value is consistent with the lower limit of 6×10^{24} cm^{-2} found with ALMA observations by Aalto et al. (2016). An obscured AGN is thus the most likely explanation for the observed properties of the NGC 1377 nucleus.

4.3. Is the AGN quenching star formation in NGC 1377?

In a deep survey of radio sources in the *Chandra* Deep Field South, Padovani et al. (2011) found that the evolution of the radio emission from radio-quiet AGN up to a redshift of $z \sim 2.3$ is indistinguishable from that of star-forming galaxies, which suggests that most of the emission in radio-quiet AGN must come from star formation. If we assume that all the radio emission from NCG 1377 is powered by star formation, the models of Figs. 8a and b result in an upper limit for the SFR of a few 0.01 $M_\odot$ yr^{-1}. This value is more than 20 times lower than the SFR inferred from the SK relation of Sect. 3.5 and could be even lower if we consider that part of the radio emission may be coming from the AGN and not from star formation. The galaxy thus seems to be forming stars at a much lower rate than the local main sequence.

Feedback from an AGN has been proposed to have a deep effect on the star formation in the host galaxies. In particular, it has been suggested that even low-power AGN could drive massive molecular outflows which could inhibit or shut down entirely star formation in the core of galaxies (e.g., Cicone et al. 2014). In a recent study of the low-power AGN host NGC 1266, a system which is very similar to NGC 1377, Alatalo et al. (2015) find a SFR 50 to 150 times lower than the Schmidt-Kennicutt value. The apparent suppression of star formation may be due to the injection of turbulence by the AGN outflow, which could stabilize the molecular gas against gravitational collapse.

Following Alatalo et al. (2015), the radial turbulent velocity needed in order to stabilize a spherical molecular bulge is of the order of the free-fall velocity

$$v_{ff} = \sqrt{\frac{3GM_{gas}}{5R}}, \tag{10}$$

where M_{gas} is the gas mass enclosed in the radius R. For the inner 60 pc of NGC 1377 we find $v_{ff} \approx 50$ km s^{-1}, which is very close to the CO 3-2 line width of 50−60 km s^{-1} measured in the core of NGC 1377 by Aalto et al. (2016). This result suggests that turbulent motions may indeed stabilize the gas against gravitational collapse and hence inhibit star formation in the galaxy nucleus. A velocity dispersion of 50 km s^{-1} could be easily maintained by turbulence generated by the observed AGN outflow (e.g., Appleton et al. 2006), which has a terminal velocity of the order of 240−850 km s^{-1}. Turbulent energy dissipation would be consistent with the bright MIR H_2 emission observed by Roussel et al. (2006). We note however that there is now significant observational evidence (e.g., Onodera et al. 2010; Xu et al. 2015) that the SK relation may be scale-dependent and may break down at giant molecular cloud (GMC, ≈100 pc) scales. The order-of-magnitude difference between the measured SFR and the SK-estimated value in the 60 pc nucleus of NGC 1377 may thus be consequence of the SK breakdown at small scales rather than an indication of negative feedback from an AGN. In order to disentangle the two scenarios, observations at higher angular resolution are needed. These would allow us to assess the contribution of the AGN to the radio flux and derive a more accurate measurement of the SFR surface density.

4.4. Is the B component associated with NGC 1377?

A search of publicly available astronomical databases (*Simbad*[3], *NED*[4]) found no identification of the B radio component as part of an independent Galactic or extragalactic object. The steep radio index makes it unlikely for the B component to be associated with a Galactic source, and optical images do not show any indication of foreground emission. There is however the possibility that the B component may be associated with another radio-faint galaxy.

Following Condon et al. (1998), the probability that the nearest unrelated radio source lies within angular distance r of any position is given by

$$P(<r) = 1 - \exp\left(-\pi\rho r^2\right), \tag{11}$$

where ρ is the number density of radio sources. A large-area survey of sub-mJy 1.4 GHz sources (ATESP, Prandoni et al. 2000) detected 2960 individual sources brighter than 79 μJy in a 26 deg^2 field, corresponding to a $\rho_{ATESP} \simeq 113$ sources/deg^2. The B component has an L-band peak flux of 101 μJy, which is comparable to the limiting sensitivity of the ATESP survey. If we assume $\rho = \rho_{ATESP}$ and $r = 4\farcs5$, the probability that the B component is not associated with NGC 1377 but with another extragalactic source is then $P(<4\farcs5) = 5 \times 10^{-4}$.

This probability becomes even lower if we consider the alignment of the B component with the blue-shifted part of the CO outflow detected by Aalto et al. (2012), as shown in Fig. 10 and further discussed in the next section.

[3] http://simbad.u-strasbg.fr/simbad/
[4] https://ned.ipac.caltech.edu/

4.5. The B component: a hot-spot in the AGN jet?

The B component shows an optically-thin synchrotron radio spectrum, soft X-ray emission, and is aligned with the blue-shifted part of the molecular outflow detected by Aalto et al. (2012, 2016) (Fig. 10). If an AGN is indeed powering NGC 1377, the B component may be associated with a hot-spot in an AGN jet. Hot-spots are defined as bright compact regions at the end of quasar radio lobes and are usually explained as strong shocks generated by the impact of the relativistic jet with the slow-moving plasma in the lobes (e.g., Blandford & Rees 1974; Meisenheimer et al. 1989). Both radio and X-ray emission are generated by synchrotron losses as particles are accelerated in the shock. Soft X-ray emission is mostly associated with radio-faint hot-spots, where the magnetic field is low enough to allow particles to be accelerated to X-ray energies (e.g., Hardcastle et al. 2016). In NGC 1377 we detect only the blue-shifted side of the putative jet, with no detection of a symmetric counter-jet. Asymmetries in the hot-spot positions along a jet are commonly observed (e.g., Mundell et al. 2003; Hardcastle et al. 2016) and may be due to inhomogeneities in the ISM or magnetic field downstream the jet. The non-detection of a counter-jet hot spot may also indicate that the mean bulk jet speed is still relativistic at the B position, which would enhance the emission of the jet-side hot-spot versus the counter-jet-side one.

Even if they do not contribute significantly to the bolometric luminosity of the galaxy as in radio-loud sources, relativistic jets are commonly observed in radio-quiet *radiative-type* AGNs (e.g., Heckman & Best 2014) with high accretion efficiency (such as the putative AGN in NGC 1377, see Sect. 4.2) and can have a deep impact on the gas kinematics (e.g., Veilleux et al. 2005). Entrainment of cold molecular gas by a precessing relativistic jet has been suggested by Aalto et al. (2016) to explain the extreme collimation of the CO 3−2 outflow in NGC 1377. Hydrodynamical simulations (e.g., Wagner et al. 2012) show that 10−40% of the AGN jet energy can be transferred to the entrained molecular material. The measured mechanical luminosity of the CO outflow ($L_{\rm mech} \sim 10^{42}$ erg s^{-1}) is thus a lower limit to the total luminosity of the jet. In radio galaxies, a loose correlation between the total monochromatic power of the AGN at 1.4 GHz and the luminosity of the relativistic jet is observed (e.g., Eq. (16) in Bîrzan et al. 2008). By applying this correlation to the measured 1.5 GHz flux of NGC 1377 ($P_{1.5\ \rm GHz} \sim 3 \times 10^{26}$ erg s^{-1}/Hz) the expected luminosity of the jet should be of the order of $\sim 10^{42}$ erg s^{-1}, which is similar to the measured mechanical luminosity of the CO outflow (*massive jet* case, see Sect. 3.6.4). Also, the estimated X-ray luminosity of the B component ($10^{38}-10^{39}$ erg s^{-1}, see Sect. 3.7) could be easily be powered by such a jet. However, the correlation between AGN power and radio lobe luminosity has a large scatter and recent studies (e.g., Godfrey & Shabala 2016) suggest that this correlation may be very weak when the jet energy is dissipated along its path, for example by driving shocks.

The morphology and energetics of the radio and X-ray emission in NGC 1377 are consistent with an AGN+jet system. Radio observations at higher resolution will help to confirm the presence of a jet and to study the interactions between the relativistic plasma and the entrained molecular material.

5. Conclusions

We report radio and X-ray observations of NGC 1377, the most extreme FIR-excess galaxy known to date, in which a highly collimated molecular outflow has recently been found. Our results suggest that the morphology and energetics of the radio, X-ray, and molecular line emissions point toward a radio-faint AGN+jet system explanation, rather than a nascent starburst as previously proposed to interpret the observed properties of the galaxy. Our main results are:

- We obtained the first detection of the cm-wave radio continuum in NGC 1377. Both the 1.5 and 10 GHz emission show two components, peaking on the galaxy nucleus and 4.″5 ∼ 500 pc to the south-west. The two radio components have a steep spectral index $\alpha \sim 0.5-0.7$, consistent with optically thin synchrotron emission.
- Soft X-rays emission (0.3−7 keV) is tentatively detected for the first time in NGC 1377 by *Chandra*. The emission is peaked at the position of the off-nucleus radio component with no detection at the galaxy's center.
- We confirm the extreme FIR excess of the galaxy, with a $q_{\rm FIR}$ of 4.2 which deviates for more than 7σ from the radio-FIR correlation ($q_{\rm FIR} = 2.34 \pm 0.26$, Roussel et al. 2003).
- By comparing the observations with synthetic starburst models, we find that the SFR estimated from optically thin free-free (<0.1 $M_\odot$ yr^{-1}) falls short by one to two orders of magnitude from explaining the galaxy's IR luminosity and the mechanical luminosity of the CO outflow. We conclude that a young starburst cannot reproduce all the observed properties of NGC 1377.
- We estimate that a SMBH of 10^6 $M_\odot$ accreting at nearly Eddington rates may reproduce the observed IR luminosity and outflow energy. Such an AGN would be extremely radio-faint, with $R \equiv L_{\rm 5GHz}/L_{4400\ \text{Å}} \approx 0.02$.
- The SFR density measured by radio observations is more than 20 times lower than the SFR inferred from the Schmidt-Kennicutt relation. We find that a turbulent velocity of 50 km s^{-1} would be sufficient to stabilize the galaxy bulge against gravitational collapse and inhibit star formation. This value is similar to the velocity dispersion of CO observations. We suggest that turbulent feedback from the AGN may be inhibiting star formation in the bulge of NGC 1377.
- The radio and X-ray emission from the off-nucleus component are consistent with the presence of a relativistic jet hot-spot. We suggest that this structure may be revealing the presence of a radio counterpart to the CO 3−2 highly collimated outflow.

Acknowledgements. F.C. acknowledges support from Swedish National Science Council grant 637-2013-7261. A.L. acknowledges support from the ERC Advanced Grant "*FEEDBACK*". R.H.I., M.A.P.T. and A.A. acknowledge support from the Spanish MINECO through grants AYA2012-38491-C02-02 and AYA2015-63939-C2-1-P.

References

Aalto, S., Muller, S., Sakamoto, K., et al. 2012, A&A, 546, A68
Aalto, S., Costagliola, F., Muller, S., et al. 2016, A&A, 590, A73
Alatalo, K., Lacy, M., Lanz, L., et al. 2015, ApJ, 798, 31
Appleton, P. N., Xu, K. C., Reach, W., et al. 2006, ApJ, 639, L51
Arnaud, K. A. 1996, in Astronomical Data Analysis Software and Systems V, eds. G. H. Jacoby, & J. Barnes, ASP Conf. Ser., 101, 17
Bell, E. F. 2003, ApJ, 586, 794
Bîrzan, L., McNamara, B. R., Nulsen, P. E. J., Carilli, C. L., & Wise, M. W. 2008, ApJ, 686, 859
Blandford, R. D., & Rees, M. J. 1974, MNRAS, 169, 395
Cicone, C., Maiolino, R., Sturm, E., et al. 2014, A&A, 562, A21
Condon, J. J. 1992, ARA&A, 30, 575
Condon, J. J., Cotton, W. D., Greisen, E. W., et al. 1998, AJ, 115, 1693

Costagliola, F., Aalto, S., Sakamoto, K., et al. 2013, A&A, 556, A18
Croton, D. J., Springel, V., White, S. D. M., et al. 2006, MNRAS, 365, 11
Daddi, E., Elbaz, D., Walter, F., et al. 2010, ApJ, 714, L118
Dahmen, G., Huttemeister, S., Wilson, T. L., & Mauersberger, R. 1998, A&A, 331, 959
Dale, D. A., Gil de Paz, A., Gordon, K. D., et al. 2007, ApJ, 655, 863
Genzel, R., Tacconi, L. J., Gracia-Carpio, J., et al. 2010, MNRAS, 407, 2091
Godfrey, L. E. H., & Shabala, S. S. 2016, MNRAS, 456, 1172
Graham, A. W., Onken, C. A., Athanassoula, E., & Combes, F. 2011, MNRAS, 412, 2211
Hardcastle, M. J., Lenc, E., Birkinshaw, M., et al. 2016, MNRAS, 455, 3526
Heckman, T. M., & Best, P. N. 2014, ARA&A, 52, 589
Helou, G., Soifer, B. T., & Rowan-Robinson, M. 1985, ApJ, 298, L7
Imanishi, M. 2006, AJ, 131, 2406
Imanishi, M., Nakanishi, K., Tamura, Y., & Peng, C.-H. 2009, AJ, 137, 3581
Janssen, R. M. J., Röttgering, H. J. A., Best, P. N., & Brinchmann, J. 2012, A&A, 541, A62
Kellermann, K. I., Sramek, R., Schmidt, M., Shaffer, D. B., & Green, R. 1989, AJ, 98, 1195
Kennicutt, Jr., R. C. 1998, ARA&A, 36, 189
Kennicutt, R. C., & Evans, N. J. 2012, ARA&A, 50, 531
Kroupa, P. 2001, MNRAS, 322, 231
Leitherer, C., Schaerer, D., Goldader, J. D., et al. 1999, ApJS, 123, 3
McAlpine, K., Prandoni, I., Jarvis, M., et al. 2015, Advancing Astrophysics with the Square Kilometre Array (AASKA14), PoS 174, 83
McMullin, J. P., Waters, B., Schiebel, D., Young, W., & Golap, K. 2007, in Astronomical Data Analysis Software and Systems XVI, eds. R. A. Shaw, F. Hill, & D. J. Bell, ASP Conf. Ser., 376, 127
Meisenheimer, K., Roser, H.-J., Hiltner, P. R., et al. 1989, A&A, 219, 63
Mundell, C. G., Wrobel, J. M., Pedlar, A., & Gallimore, J. F. 2003, ApJ, 583, 192
Murphy, E. J., Condon, J. J., Schinnerer, E., et al. 2011, ApJ, 737, 67
Onodera, S., Kuno, N., Tosaki, T., et al. 2010, ApJ, 722, L127
Padovani, P., Miller, N., Kellermann, K. I., et al. 2011, ApJ, 740, 20
Prandoni, I., Gregorini, L., Parma, P., et al. 2000, A&AS, 146, 41
Roussel, H., Helou, G., Beck, R., et al. 2003, ApJ, 593, 733
Roussel, H., Helou, G., Smith, J. D., et al. 2006, ApJ, 646, 841
Sakamoto, K., Aalto, S., Costagliola, F., et al. 2013, ApJ, 764, 42
Sikora, M., Stawarz, Ł., & Lasota, J.-P. 2007, ApJ, 658, 815
Spoon, H. W. W., Marshall, J. A., Houck, J. R., et al. 2007, ApJ, 654, L49
Temi, P., Brighenti, F., & Mathews, W. G. 2009, ApJ, 707, 890
Vasudevan, R. V., & Fabian, A. C. 2007, MNRAS, 381, 1235
Veilleux, S., Cecil, G., & Bland-Hawthorn, J. 2005, ARA&A, 43, 769
Wagner, A. Y., Bicknell, G. V., & Umemura, M. 2012, ApJ, 757, 136
Xu, C. K., Cao, C., Lu, N., et al. 2015, ApJ, 799, 11
Yun, M. S., Reddy, N. A., & Condon, J. J. 2001, ApJ, 554, 803